ACS Photonics
pubs.acs.org/journal/apchd5 Article

Efficient Finite Element Modeling of Light Scattering in Symmetric Structures: A Nondegenerate Case

Jingwei Wang, Lida Liu, Yuhao Jing, Zhongfei Xiong,* Dominik Kowal, and Yuntian Chen*

Cite This: *ACS Photonics* 2025, 12, 2053−2061 Read Online

ACCESS | Metrics & More | Article Recommendations | Supporting Information

ABSTRACT: In recent years, advancements in optical scattering of nanostructures have significantly driven the development of telecommunications, medical imaging, detection, and novel light sources. However, due to the structural complexity of nanostructures, particularly metasurfaces and metamaterials, traditional methods of full-wave modeling for simulating optical scattering face substantial challenges due to increased degrees of freedom. In this work, we propose a symmetry-adapted finite element method to reduce the computational domain and enhance the efficiency of optical scattering simulations. By introducing the concepts of symmetry group and projection operator, we offer a formal and rigorous framework for decomposing the original problem, i.e., the incident condition, boundary constraints, and the finite element method implementation in decoupled subtasks. To demonstrate its broad applicability, we present three numerical examples: the enhancement of light confinement via quasi-bound states in the continuum in a photonic crystal slab, the scattering cross sections of incident configurations, and the calculation of transmission spectra in the metasurface. These examples illustrate the use of the symmetry finite element method under different symmetry conditions, including mirror symmetry, rotational symmetry, and the combination of Bloch's theorem. Our method significantly reduces computation time and memory usage, thereby greatly improving the computational efficiency. Given the universality of symmetry principles, our method has important applications in the optical analysis and design of symmetric photonic devices, especially for symmetric yet large-sized optical structures.

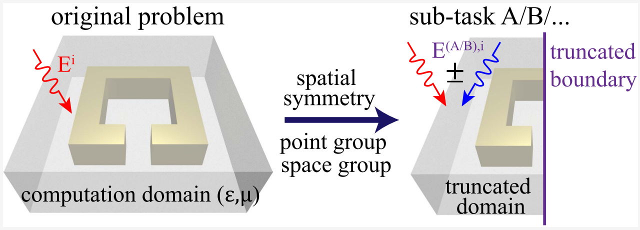

KEYWORDS: *numerical calculations, finite element method, group theory, optical scattering problem, photonic crystal, metasurface*

■ INTRODUCTION

Simulation and modeling using numerical methods is one of the key approaches in the field of photonics, ranging from studying both fundamental optics and applied branches such as the design, development, and optimization, yet with increased needs for highly efficient numerical algorithms for complex photonic components.[1−7] Especially, for numerical modeling methods such as the finite element method (FEM) and the finite difference method (FDM), the computational load for photonic devices is closely related to the size of the computational domain, which affects the number of degrees of freedom (DOFs) that need to be solved. Notably, many photonic devices are or at least can be approximated to be symmetric, allowing the computational domain to be reduced to a small portion of the original devices by the symmetry principle and thus significant reduction of the DOFs. Indeed, in the mode analysis of optical waveguides, mirror symmetry is utilized to model half or a quarter of the device.[8,9] This method essentially employs symmetry groups to decompose the original mode analysis problem into fully decoupled subtasks, with each subtask corresponding to solving for a specific type of mode.[10] Evident from those existing work,[10−16] the domain reduction from symmetry argument has been proved to be an effective approach to model symmetric and complex photonic devices.

As for light scattering in symmetric structure, its additional challenge compared to that in the modal analysis or eigenfrequency problems is the symmetry breaking of the overall problem due the external excitations, i.e., plane waves or point dipoles. In this regard, the domain reduction techniques used in photonic modal problems cannot be transplanted to light scattering problem directly since the external excitation hardly has the identical symmetry as the photonic devices. To solve the symmetry incompatibility between the external excitation and the structure symmetry, Yangxin Ou[17] and Sergei Gladyshev[16] matched continuous rotational or translational symmetry by Fourier expansion of the external excitations. Henrik Mntynen and colleagues explored the application of mirror symmetry in FEM using group theory.[14] However, those works are incomplete and rather limited as they lack the

Received: December 12, 2024
Revised: March 18, 2025
Accepted: March 18, 2025
Published: March 27, 2025

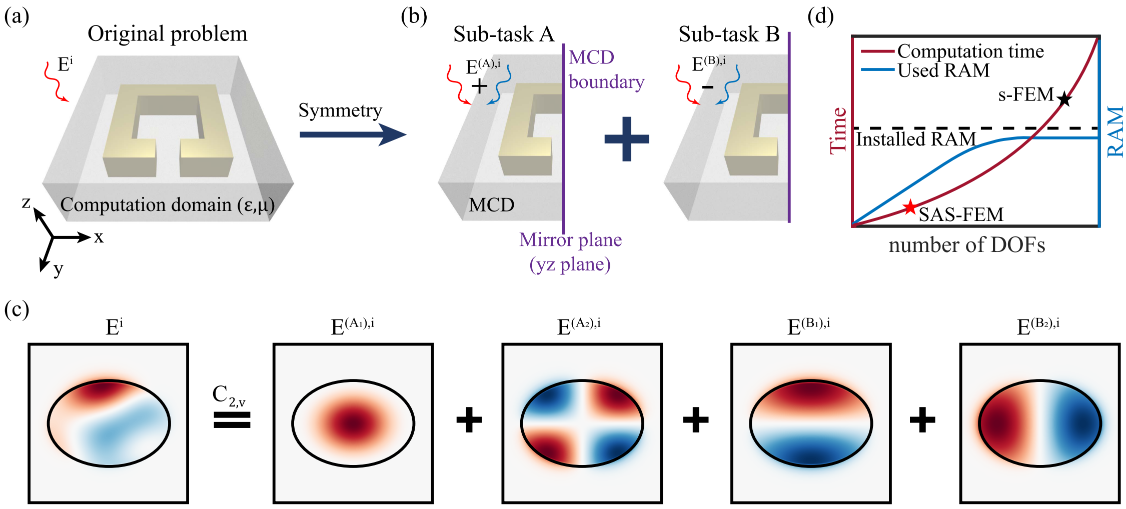

Figure 1. Schematic of symmetry-adapted FEM for the light scattering problem. (a) s-FEM for solving an optical scattering problem with mirror symmetry. The optical scattering problem consists of computation domain, incident light, and boundary conditions. (b) Symmetry-adapted FEM for solving an optical scattering problem with the mirror symmetry. Half of the entire domain is modeled (as MCD), and the original problem is decomposed into several subtasks, each with different MCD boundary constraints and subincident fields. (c) Arbitrary incident field is decomposed into four subincident fields that adhere to the symmetries of the C_{2v} point group. (d) RAM usage and total computational time versus the number of DOFs.

capability to extend to other complex symmetric structures. Especially, the critical issues such as constructing symmetric boundary constraints and reconstructing the entire domain's electric field from the truncated domain in a systematic manner also remain unresolved.

In this work, we systematically investigate and propose a symmetry-adapted FEM framework and its application in optical scattering problems. This method addresses the issue of the mismatch between the broken symmetry of the external excitation and the structure symmetry by employing projection operators to decompose any incident field into orthogonal and complete subincident fields that conform to the symmetry group. As such, the original scattering problem is able to be decomposed into several independent subtasks based on the symmetry group. Each of the incident and scattering fields of each subtask satisfies the symmetry conditions, allowing for the truncation of the computational domain and thus reducing the DOFs. By symmetry projection operators, we derive the symmetry constraints on boundaries and establish the relationship between the electric field in the truncated domain and other domains, facilitating the reconstruction of the electric field in the complete domain. Three numerical examples are demonstrated to show that our approach is valid for mirror symmetry, rotational symmetry, and discrete translation symmetry. Comparisons with the standard finite element method (s-FEM) verify the validity and efficiency of our proposed method, especially for large-scale devices. It should be noted that in the scattering numerical computation, we only excite the nondegenerate mode for illustration, as indicated in the title of our paper. This work focuses on point group and symmorphic space group symmetries, with more complex nonsymmorphic space group symmetries reserved for future investigations.

SYMMETRY-ADAPTED FINITE ELEMENT METHOD FOR A LIGHT SCATTERING PROBLEM

In the implementation of the s-FEM to compute optical scattering problems, it is essential to define the computational domain according to the device's structure and specify the incident field and boundary conditions. Figure 1a presents a schematic diagram of s-FEM modeling for a mirror-symmetric structure with an obliquely incident light $E^i(r)$. In the computational domain, the total electric field $E(r)$ satisfies the vector wave equation,

$$\nabla \times \bar{\mu}_r^{-1} \nabla \times E(r) - k_0^2 \bar{\varepsilon}_r E(r) = 0 \quad (1)$$

where $\nabla \times$ is the curl operator, $\bar{\mu}_r$ is the relative permeability, $\bar{\varepsilon}_r$ is the relative permittivity, k_0 is the wavenumber in a vacuum, $r = (x, y)^T/(x, y, z)^T$ represents the spatial coordinates in two/three dimensions. In the optical scattering problem, the total field $E(r)$ is the sum of the incident field $E^i(r)$ and the scattered field $E^s(r)$, i.e., $E(r) = E^i(r) + E^s(r)$, wherein $E^s(r)$ is the dependent variables that we intend to solve.

By leveraging the symmetry of the structure, characterized by $\varepsilon_r(r)$ and $\mu_r(r)$, we can model only a portion of the overall computation domain termed the minimum computation domain (MCD), where the newly formed boundary is called the MCD boundary, as shown in Figure 1b. For mode analysis or eigen frequency problems,[18,19] the MCD can be obtained through structural symmetry alone. As for scattering problems, both the scattered field $E^s(r)$ and the total field $E(r)$ exhibit the structure symmetry only if the incident field $E^i(r)$ and the structure geometry have identical symmetry. This indicates that the MCD can be obtained only if the incident field fulfills the structure symmetry exactly. To this end, we decompose the original incident field into a series of subincident fields adapted to the structure's symmetry, i.e., each subincident field exhibits symmetric or antisymmetric properties consistent with mirror symmetry. Importantly, by symmetry arguments, any arbitrary incident field can be decomposed into a series of subincident fields that adhere to a given symmetry group. The symmetry group ensures the closure between the subincident fields and the original field. As an example illustrated in Figure 1c, the incident field is decomposed into four subincident fields that conform to the C_{2v} symmetries using the C_{2v} point group. Accordingly, due to the linearity of eq 1, the original scattering

https://doi.org/10.1021/acsphotonics.4c02474
ACS Photonics 2025, 12, 2053−2061

problem can be decomposed into multiple subtasks, each with a common MCD but different subincident fields and boundary conditions. This method is referred to symmetry-adapted FEM for light scattering problems, i.e., symmetry-adapted scattering FEM (SAS-FEM). The implementation procedure of SAS-FEM consists of four steps,

1. Identify the structure's symmetry, identify the symmetry group, and determine the corresponding character table.
2. Decompose the original problem into multiple subtasks based on the character table, and divide the incident field into subincident fields using projection operators.
3. Truncate the computational domain to the MCD and derive the boundary constraints for different subtasks based on symmetry.
4. Solve all subtasks and restore the solution to the original problem using symmetry principles.

Although the SAS-FEM involves multiple subtasks, the DOFs in each subtask are significantly reduced. In solving large sparse linear equations, the computational efficiency does not increase linearly with the DOFs. As shown in Figure 1d, halving the DOFs enhances computational efficiency by a factor of more than 2-fold. This improvement becomes particularly significant as the used random-access memory (RAM) approaches the computer's installed RAM. Additionally, these subtasks are entirely decoupled, allowing for further improved computational efficiency through the application of parallel computing techniques. Consequently, SAS-FEM remarkably improves computational efficiency compared to s-FEM, particularly in terms of computation time and RAM usage. This improvement is especially notable in large-scale simulations.

Scattering Problem Decomposition. The decomposition of the original scattering problem and the incident field, as well as the boundary constraints, all depend on the given structure symmetry. Thus, it is essential to first identify the symmetry properties of the structure geometry, which can be analyzed following the standard procedure given by International Table for Crystallography.[20] The detailed discussions can be referred to in our previous work.[21] Specifically, nonperiodic structures, such as the one in Figure 1a and symmetric scatterers, typically satisfy a given point group. In contrast, periodic structures, such as photonic crystals and the unit cell of metasurfaces/metamaterials, require the use of wave vector groups. After determining the symmetry group of the structure, the optical scattering problem can be decomposed into a number of subtasks. Meanwhile, the subincident fields for these subtasks can be derived from the original incident field through the decomposition of the original problem and incident field with the assistance of the character table and projection operators. The symmetry group and its character table ensure the equivalence between subtasks and the original problem, while the projection operators facilitate a more general and operable decomposition of the incident field.

We use the structure with the C_s point group shown in Figure 1a as an example to illustrate the basic principle of SAS-FEM. The corresponding character table is provided in Table 1, decomposing the original problem into two subtasks, A and B, corresponding to the irreducible representations of the C_s group. The electric fields in both subtasks adhere to the mirror symmetry σ_{yz}, but they follow opposite boundary constraints. Specifically, the electric field in subtask A is mirror-symmetric,

Table 1. Character Table for C_s Point Group

	E	σ_{yz}
A	1	1
B	1	−1

whereas the electric field in subtask B is mirror antisymmetric. Accordingly, subtask A/B adheres to the boundary constraints of perfect electric conductor (PEC)/perfect magnetic conductor (PMC) at the MCD boundary. The basic concepts of character, character table, and irreducible representations and the applications of group theory can be found in the textbooks.[22,23]

Projection Operator and the Incident Field Decomposition. The electric fields associated with all of the irreducible representations in a group form a complete set of orthogonal bases. These bases can describe any electric field in an optical structure that adheres to the symmetry group according to the character table. Projection operators in group theory can project any electric field onto the orthogonal bases. Consequently, by employing projection operators, any incident field can be decomposed into subfields that adhere to the symmetry constraints of the specific irreducible representations. This method effectively addresses the issue of incompatibility between the incident field and the structure. For self-consistency, the projection operator is given as follows, see details in the textbooks,[22,23]

$$\mathrm{P}^{(\Gamma)} = \frac{\mathrm{l}_n}{\mathrm{h}} \sum_{\mathrm{O}} \chi^{(\Gamma)}(\mathrm{O})^* \mathrm{P}_{\mathrm{O}} \tag{2}$$

where Γ represents the irreducible representation of the subincident field $\mathrm{E}^{(\Gamma),i}(\mathrm{r})$ and the corresponding subtask, O donates the symmetry in the group, $\mathrm{P_O}$ is the symmetry operation, $\chi^{\Gamma}(\mathrm{O})$ is the corresponding character, l_n is the dimension of the n-th irreducible representation of the symmetry group with order h (the number of symmetry operations in the group), and * denotes the complex conjugate.

The projection operator decomposition of the incident field consists of two steps. The first step involves constructing a complete basis using the symmetry operations of the group. The second step is to reconstruct the basis from the first step into a new basis, which is exactly the electric field corresponding to the irreducible representation, as tabulated in the character table. The new basis thus formed not only is orthogonal and complete but also adheres to the symmetry constraints of the symmetry group. For instance, we examine the decomposition of the projection operator for left-handed circularly polarized (LCP) light E^i incident on a scatterer exhibiting C_s group symmetry, as illustrated in Figure 2. According to Table 1, point group C_s consists of two distinct symmetry operations $\mathrm{P_E}$ and $\mathrm{P}_{\sigma_{yz}}$. Hence, two bases $\mathrm{P_E E}^i$ and $\mathrm{P}_{\sigma_{yz}}\mathrm{E}^i$ can be derived, corresponding to LCP and right-handed circularly polarized (RCP) light, respectively. Subsequently, based on the linear combination of the characters, two new bases that satisfy the symmetry constraints of two irreducible representations are reconstructed:

$$\mathrm{E}^{(\mathrm{A}),i} = \mathrm{P}^{(\mathrm{A})}\mathrm{E}^i(\mathrm{r}) = \frac{1}{2}[\mathrm{P_E}\mathrm{E}^i(\mathrm{r}) + \mathrm{P}_{\sigma_{yz}}\mathrm{E}^i(\mathrm{r})] \tag{3a}$$

$$\mathrm{E}^{(\mathrm{B}),i} = \mathrm{P}^{(\mathrm{B})}\mathrm{E}^i(\mathrm{r}) = \frac{1}{2}[\mathrm{P_E}\mathrm{E}^i(\mathrm{r}) - \mathrm{P}_{\sigma_{yz}}\mathrm{E}^i(\mathrm{r}))] \tag{3b}$$

https://doi.org/10.1021/acsphotonics.4c02474
ACS Photonics 2025, 12, 2053−2061

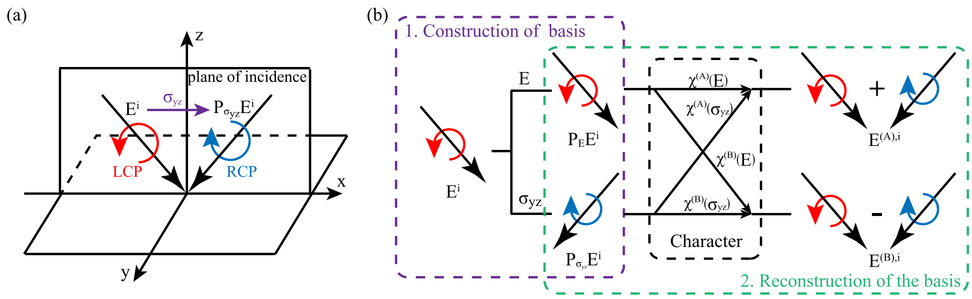

Figure 2. Schematic of decomposing the incident field by mirror symmetry. (a) LCP light that is incident obliquely along the positive x-axis transforms into RCP light incident obliquely along the negative x-axis under mirror symmetry σ_{yz}. (b) Projection operators corresponding to the C_s point group can decompose the LCP light. By combining the LCP light and RCP light according to the characters, a pair of subincident fields that satisfy the C_s point group symmetry can be obtained.

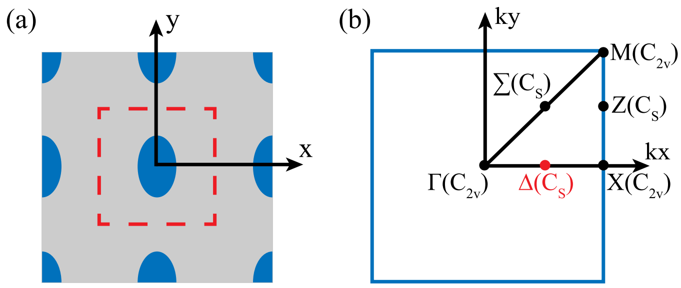

Figure 3. Symmetry group and boundary constraints of periodic structures. (a) Schematic diagram of 2D periodic structure with wallpaper group p2 mg. (b) First Brillouin zone and the wave vector groups at high-symmetry lines/points of the structure in panel (a). (c) Implementation of SAS-FEM for the structure in panel (a) utilizes Bloch's theorem alongside mirror symmetry. The boundaries b_0 and b_1 continue to satisfy Bloch's theorem, whereas m_0 and m_1 adhere to both the Bloch's theorem and mirror symmetry constraints.

where $E^{(A),i}$ and $E^{(B),i}$ form an orthogonal pair of bases and represent the subincident fields corresponding to the irreducible representations A and B obtained through decomposition. When the incident field $E^i(r)$ fulfills all the symmetries of a given irreducible representation, only a subtask requires computation. When the incident field $E^i(r)$ conforms to only some symmetries, the partially projected subincident fields are zero. Consequently, only the subtasks associated with the nonzero subincident fields need to be carried out. Theoretically, any incident field can be decomposed into subincident fields corresponding to individual irreducible representations, provided the character table of the optical structures symmetry is available. The greater the number of irreducible representations possessed by the symmetry group of the structure, the more subtasks can be decomposed. This decomposition can enhance the benefits of parallel computation, thereby improving the computational efficiency.

The concept of employing orthogonal and complete basis decomposition that admits symmetry for electric fields is not new. Both the multipole decomposition in Mie scattering theory and the Fourier series expansion[16] of electric fields are founded upon this principle for spherical scatterers. In polar coordinates, the Fourier series expansion is represented by

$$E^i(r) = \sum_{m=-\infty}^{\infty} E_m(\rho, z)e^{im\phi} \tag{4a}$$

$$E_m(\rho, z) = \frac{1}{2\pi}\int_{2\pi} E^i(r)e^{-im\phi}d\phi \tag{4b}$$

The projection operator for an arbitrary rotational symmetry group C_N (where $N > 1$) and the corresponding subelectric field can be expressed as

$$\begin{aligned} P^{(\Gamma)} &= \frac{1}{N}\left[\chi^{(\Gamma)}(E)^* P_E + \sum_{m=2}^{N}\chi^{(\Gamma)}(c_m)^* P_{c_m}\right] \\ &= \frac{1}{N}\left[P_E + \sum_{m=2}^{N}\mathrm{sgn}^{(\Gamma)}(c_m)e^{iM\varphi}P_{c_m}\right] \end{aligned} \tag{5a}$$

$$E^{(\Gamma),i} = P^{(\Gamma)}E^i(r) = \frac{1}{N}\left[E^i(r) + \sum_{m=2}^{N}\mathrm{sgn}^{(\Gamma)}(c_m)e^{iM\varphi}P_{c_m}E^i(r)\right] \tag{5b}$$

where the function $\mathrm{sgn}^{\Gamma}(c_m)$ represents the sign function, which depends on the irreducible representation and the rotational symmetry operation, and can take values of either +1 or −1. φ is the rotation angle given by $2\pi/N$, and M = 1, ..., and $N-1$ is a positive integer associated with the irreducible representation of the rotational symmetry. The Fourier series and the projection operator share analogous mathematical structures, as both decompose a function into a set of orthogonal bases. However, the projection operator is a finite expansion, while the Fourier series is an infinite expansion. As N approaches infinity, the projection operator and the Fourier series become nearly identical, indicating that the Fourier series can be seen as a special case of the projection operator.

Application of Symmetry-Adapted FEM in Periodic Photonic Structures. As for periodic structures, Bloch's theorem requires that the symmetry groups used in SAS-FEM modeling be the wave vector groups rather than the point groups typically applied to individual scatterers. Figure 3a depicts a 2D ideal photonic crystal that satisfies the wallpaper group p2 mg. In reciprocal space, the symmetry groups at different wave vectors are known as wave vector groups, and

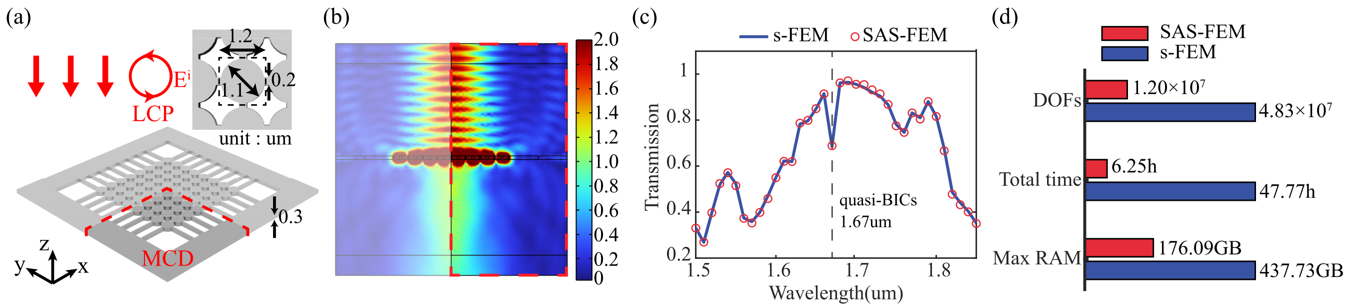

Figure 4. Numerical simulation of the 8-by-8 two-dimensional photonic crystal slab. (a) Structure of the two-dimensional photonic crystal slab with normal incident LCP light. (b) Electric field distribution obtained from simulation at a wavelength of 1.67 μm. (c) Transmission spectrum obtained from simulation. The sharp drop at 1.67 μm indicates quasi-BICs. (d) Comparison of DOFs, total time, and maximum RAM between the SAS-FEM and the s-FEM.

Figure 3b illustrates the wave vector groups at high-symmetry lines and points. As a result, the choice of symmetry group in SAS-FEM modeling of periodic structures depends on the direction (wave vector) of the incident light. Although the use of SAS-FEM depends on the direction of incidence, simulations typically concentrate solely on the electromagnetic responses in these specified directions, i.e., the high-symmetry points/lines. For instance, assuming an oblique incidence of light along the x-axis and given that the wave vector group on the high-symmetry line Δ is C_S, the original problem can be decomposed into two subtasks, A and B. We will use subtask A to detail the implementation of SAS-FEM.

Figure 3c illustrates the MCD of the periodic structure in Figure 3a. The boundaries of the MCD are denoted by b_0, b_1, m_0, and m_1, where $\hat{e}_{0/1/2}$ represents the unit tangent vector at the respective boundary. From Bloch's theorem, we can derive the constraints on boundaries b_0, b_1, m_1, and m_2,

$$E(r_{b_0}) = e^{ik_x d_x} E(r_{b_1}) \tag{6a}$$

$$E(r_{m_1}) = E(r_{m_2}) \tag{6b}$$

where d_x is the width of unit and r_{b_0, b_1, m_1, m_2} represents the coordinate of respective boundary. The symmetry constraints on the electric field can be obtained through symmetry operation P_O. For detailed information about symmetry operations, please refer to Supporting Information S1 or Xiong's work.[21] Symmetry constraints on the boundaries m_0, m_1, and m_2 can be obtained through mirror symmetry operation,

$$E(r_{m_0}) = \bar{\sigma}_{xz} E(r_{m_0}) \tag{7a}$$

$$E(r_{m_2}) = \bar{\sigma}_{xz} E(r_{m_1}) \tag{7b}$$

where $\bar{\sigma}_{xz}$ is the matrix form of the symmetry operation σ_{xz} with respect to the x−z plane mirror. Therefore, from eq 7a, we obtain $\hat{e}_0 \times E(r_{m_0}) = 0$. Similarly, from eqs 6b and 7b, we find that $\hat{e}_0 \times E(r_{m_2}) = 0$. This indicates that the PMC is satisfied on both boundaries m_0 and m_1. Similarly, for SAS-FEM in nonperiodic structures, boundary constraints are derived using point groups and their corresponding symmetry operators.

Finite Element Implementation. In FEM, the electric field is expanded using discrete basis functions $E(r) = \sum_{j=1}^{N} u_j N_j(r)$, where u_j is the DOF to be solved, $N_j(r)$ is the basis function, and N is the total number of DOFs. The boundary constraints impose restrictions on the u_j. Implementing the s-FEM procedure can lead to the matrix form of eq 1,

$$Au = b \tag{8}$$

where $u = \{u_j\}$ represents the DOFs to be solved, A is the stiffness matrix, and b is the load vector. The constraint of DOFs for the subtask A in the previous section's periodic structure can be expressed in matrix form,

$$u = Pu' \tag{9a}$$

$$P = \begin{pmatrix} I & 0 & 0 & 0 \\ 0 & I & 0 & 0 \\ 0 & e^{ik_x d_x} I & 0 & 0 \\ 0 & 0 & I & 0 \\ 0 & 0 & 0 & I \end{pmatrix} \tag{9b}$$

where $u = (u_{MCD}, u_{b_0}, u_{b_1}, u_{m_0}, u_{m_1})^T$ is the original DOFs vector, $u' = (u_{MCD}, u_{b_0}, u_{m_0}, u_{m_1})^T$ is the modified DOFs vector, P is the transformation matrix, I is the identity matrix. By using matrix operations and eq 9a, eq 8 can be rewritten as,[24]

$$P^{\dagger} A P u' = P^{\dagger} b \tag{10}$$

where $P^{\dagger}$ is the Hermitian conjugate of P. By solving eq 10, the scattered electric field for subtask A can be obtained.

RESULTS AND DISCUSSION

In this section, we validate the accuracy and efficacy of the proposed method through three numerical examples, comparing it to the s-FEM. These examples are three-dimensional scattering problems and implemented by modifying the boundary constraints in the commercial simulation software COMSOL, as detailed in Supporting Information S2 and S3. The code implementation for two-dimensional scattering problems of the SAS-FEM can be accessed through our open-source Matlab program on GitHub.[25] Both SAS-FEM and s-FEM used the same mesh size settings and identical solver configurations. All results are obtained from a local server equipped with a 96-Core CPU and 1548 GB of RAM.

Quasi-BICs in a Two-Dimensional Photonic Crystal Slab. BICs in photonic crystals significantly enhance light-matter interactions,[26,27] which are crucial for improving the efficiency and performance of photonic devices. BICs are essential in applications such as lasers,[3,28−32] nonlinear optics,[33−37] and sensors.[38−40] Currently, the BIC design primarily uses Bloch periodic boundary conditions to simulate unit cell and calculate the ideal photonic crystal's band

https://doi.org/10.1021/acsphotonics.4c02474
ACS Photonics 2025, 12, 2053−2061

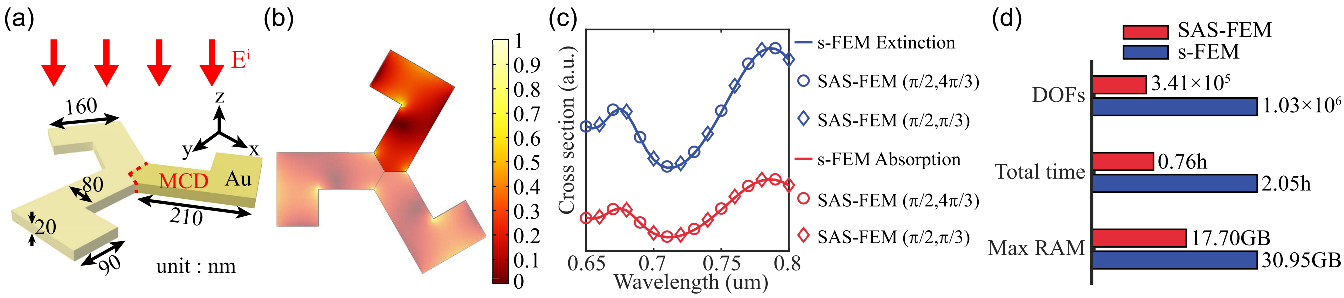

Figure 5. Numerical simulation of the scatterer. (a) Structure of a scatterer with C_3 point group symmetry. (b) Simulation results of the electric field distribution in the device cross-section at a wavelength of 0.785um. (c) Extinction and absorption spectra are shown. The solid lines represent the results of s-FEM, while the circles and diamonds depict the results of the SAS-FEM. (d) Comparison of the DOFs, total time, and maximum RAM.

structure and transmission spectrum. In practical applications, the size of photonic crystal samples is limited and often significantly larger than the working wavelength. This size discrepancy requires considerable computational resources when employing s-FEM for simulation. However, employing the SAS-FEM can significantly reduce computational resources and improve computational efficiency. For instance, we use the SAS-FEM to calculate the transmission spectrum of an 8-by-8 two-dimensional photonic crystal slab,[3] as illustrated in Figure 4a. Each unit has a width of 1.2 μm, with the cylinders having a diameter of 1.1 μm. The supporting bridge has a width of 0.2 μm, and the entire structure has a thickness of 0.3 μm. The material's refractive index is 3.6. For comparison with the results in the literature,[7,41,42] we illuminate the photonic crystal slab using LCP light at normal incidence. The structure adheres to the C_{4v} point group. In this numerical example, mirror symmetry is primarily utilized and the subgroup C_{2v} is chosen for the SAS-FEM modeling (see details in Supporting Information S3), allowing modeling of only a quarter of the complete structure. Since the LCP light satisfies the c_2 symmetry, only the incident fields of the two subtasks, B_1 and B_2, are nonzero and require calculation.

Figure 4b illustrates the electric field distribution on the cross-section of the computation domain with a vacuum wavelength λ_0 = 1.67 μm. The right section displays results calculated with the SAS-FEM, while the left section portrays results from the s-FEM with 50% transparency. We calculate the transmission spectrum over λ_0 range of 1.5 to 1.85 μm and compare the results of the SAS-FEM (red circles) with those of the s-FEM (blue line). Figure 4c presents the transmission spectrum. The excellent match between the blue line and red dots demonstrates the accuracy and robustness of the SAS-FEM. At λ_0 = 1.67 μm, and there is a notable decline in transmissivities, which implies the presence of quasi-BICs.[43] In this scenario, a significant portion of the incident photons become trapped, thereby inhibiting light transmission. As shown in Figure 4b, this quasi-BIC state induces a strong resonance within the photonic crystal slab, substantially enhancing the optical field. Figure 4d compares the number of DOFs, total computation time, and maximum RAM between the s-FEM and the SAS-FEM. The SAS-FEM reduces the number of DOFs to 1/4 of those required by the s-FEM and increases the calculation speed by a factor of 8, significantly enhancing computational efficiency. Furthermore, our local server, with a maximum memory of 1548 GB, eliminates the memory wall during computations. In situations where RAM is limited, the computation time for the s-FEM will significantly increase, further highlighting the superiority of the SAS-FEM.

Rotational Symmetry Scatterer with Dispersive Material. Optical scattering theory is fundamental in the field of optics.[44−49] This research focuses on global properties, such as total absorption and scattering cross sections, as well as local properties, including local scattering cross sections and angular polarization distributions, which are essential for simulating scattering problems. Most scatterers in these studies exhibit rotational symmetry,[48,49] allowing for effective analysis using the above SAS-FEM. For instance, Figure 5a illustrates a scatterer with the C_3 point group, consisting of gold and employing the Brendel-Bormann model. Here, the incident field is characterized using the Poincar sphere, involving elliptically polarized light created by LCP light and RCP light, described as $E^i(\chi, \psi) = \cos(\pi/4-\chi/2)e^{-i\psi/2}L + \sin(\pi/4-\chi/2)e^{i\psi/2}R$, which serves as the incident field. L and R represent LCP light and RCP light of unit intensity. By leveraging C_3 point group symmetry, only one-third of the structure needs to be modeled and calculated (see details in Supporting Information S4). Figure 5b displays the normalized electric field distribution in the central cross-section of the structure at a wavelength of 0.785 μm with incident field $E^i(\pi/2, \pi/3)$. The results in the upper-right corner, obtained using the SAS-FEM, demonstrate consistency with those obtained from the s-FEM applied in other domains.

The absorption and extinction spectra are calculated in the wavelength range from 0.65 to 0.8 μm. The incident fields are set as $E^i(\pi/2, 4\pi/3)$ and $E^i(\pi/2, \pi/3)$. As shown in Figure 5c, the blue line represents the extinction spectrum calculated by s-FEM, while the red line represents the absorption spectrum. For the SAS-FEM, the case for $E^i(\pi/2, 4\pi/3)$ is denoted by circles, and the case for $E^i(\pi/2, \pi/3)$ is depicted by diamonds. The results demonstrate an excellent agreement between the SAS-FEM and the s-FEM. Moreover, the consistency between the absorption and extinction spectra under different elliptical polarization conditions further affirms the invariance of the structure's scattering properties.[47] Comparison of the number of DOFs, total computation time, and maximum RAM, as illustrated in Figure 5d, clearly demonstrates that SAS-FEM under rotational symmetry enhances computational efficiency by a factor of 3.

Periodic Metamaterial Absorber. Metamaterials can manipulate electromagnetic wave properties, including polarization,[50] phase, amplitude,[51] and frequency, through artificially designed subwavelength structures. They are critically important in various applications such as absorbers,[52,53]

https://doi.org/10.1021/acsphotonics.4c02474
ACS Photonics 2025, 12, 2053−2061

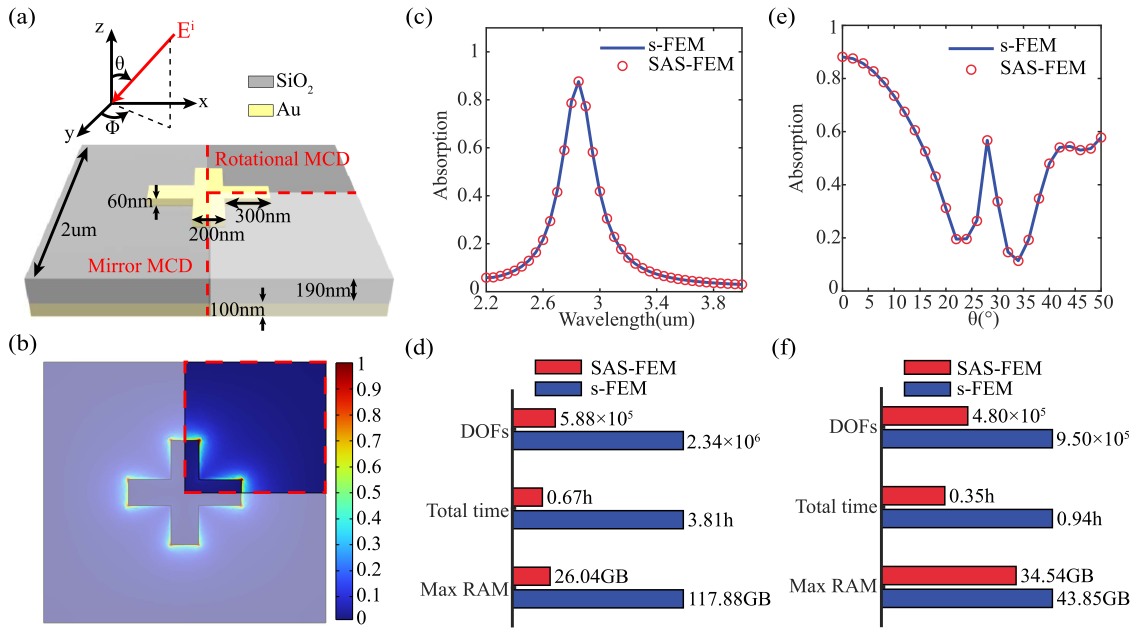

Figure 6. Numerical results of metamaterial absorber. (a) Structure of the metamaterial absorber structure. (b) The simulation results of electric field distribution in the device cross-section at a wavelength of 2.85um. (c) Absorption spectra under normal incidence. (d) Comparison of DOFs, total time, and maximum RAM under normal incidence. (e) Absorption spectra under oblique incidence. (f) Comparison of DOFs, total time, and maximum RAM under oblique incidence.

antennas,[54] AR displays,[55] and innovative lenses.[56] The design of metamaterials requires comprehensive simulations of the electromagnetic response characteristics of unit cells, for which SAS-FEM can be effectively employed. Figure 6a displays a unite cell of metamaterial absorber,[52] which consists of a 100 nm thick gold substrate, a 190 nm thick silicon dioxide layer, and a 60nm thick gold cross on top. The incident light is LCP light, and the incident direction is defined by (θ, ϕ). Under normal incidence, denoted as (0, 0), the wave vector group of the unit cell corresponds to the C_{4v}. To verify the combination of rotational symmetry and Bloch's theorem, we select the subgroup C_4 for the SAS-FEM modeling. Figure 6b presents the simulation results of electric field distribution at the central cross-section of the unit cell with a vacuum wavelength λ_0 = 2.85 μm. The results in the upper-right domain is derived from the SAS-FEM, while the remaining portion is computed using the s-FEM. Figure 6c illustrates the absorption spectrum from 2.2 to 4.0 μm, where the blue line represents the s-FEM results, and the red circles indicate the SAS-FEM results. The metamaterial absorber exhibits peak absorption for LCP light at normal incidence with the peak at 2.85 μm. Figure 6d compares the number of DOFs, total computation time, and maximum RAM. By utilizing C_4 point group symmetry, the computational domain is reduced to one-quarter of its original size, thereby enhancing computational speed 6-fold and reducing RAM usage by a factor of 4.

At λ_0 = 2.85 μm, where absorptivity is maximal under normal incidence, we investigate the effect of varying the incident angle θ from 0° to 50° on absorptivity. At these incident conditions, the wave vector group of the unit cell is C_s. The absorption is computed using the SAS-FEM, which combines mirror symmetry with Bloch's theorem. Figure 6e presents the absorption spectra, calculated from s-FEM (blue line) and SAS-FEM (red circles), which have excellent agreement with each other. At oblique incidence, the absorption efficiency of the metamaterial absorber structure for LCP light is decreased. Figure 6f compares the number of DOFs, total computation time, and maximum RAM between the SAS-FEM and the s-FEM. Since only mirror symmetry is used, the MCD is halved, thereby increasing the computing speed by approximately three times. By comparing Figure 6d,f, one concludes that selecting the symmetry group minimizes the MCD and the number of DOFs maximizes the benefits of the SAS-FEM.

CONCLUSIONS

In conclusion, this work proposes a symmetry-adapted FEM based on symmetry groups and projection operators to address light scattering problems in arbitrarily symmetric devices. By utilizing the irreducible representations and closure properties of symmetry groups, the original scattering problem is decomposed into multiple fully decoupled subtasks with fewer DOFs. The incident fields of the subtasks are derived by decomposing the incident field of the original problem through projection operators. Compared with the s-FEM, this approach significantly enhances the analysis efficiency of scattering problems while maintaining accuracy, especially for large devices. We show that the proposed method is suitable not only for point group symmetric devices such as two-dimensional photonic crystal slabs and scattering configurations but also for periodic structures such as metamaterials and metasurfaces. Given the importance of symmetry in optics, this symmetry-based method is versatile and can be easily extended from FEM to other numerical methods such as FDM and the transfer matrix method. We believe that the proposed SAS-FEM represents a significant step forward in simulating scattering problems of symmetric structures, aiding researchers in computing and designing symmetric devices more efficiently. As for the degenerate case, the general framework and numerical implementation are exactly the same as the illustrated examples, except that the MCD boundaries are more complex, which will be addressed in our future work.

https://doi.org/10.1021/acsphotonics.4c02474
ACS Photonics 2025, 12, 2053−2061

■ ASSOCIATED CONTENT

Supporting Information

The Supporting Information is available free of charge at https://pubs.acs.org/doi/10.1021/acsphotonics.4c02474.

(S1) Symmetry operation and constraint of electric field. (S2) Finite element modeling with mirror symmetry in COMSOL. (S3) Finite element modeling with rotation symmetry in COMSOL. (S4) Accuracy analysis of symmetry-adapted scattering FEM (PDF)

■ AUTHOR INFORMATION

Corresponding Authors

Zhongfei Xiong − *School of Optical and Electronic Information, Huazhong University of Science and Technology, Wuhan 430074, People's Republic of China*; Email: xiongzf94@outlook.com

Yuntian Chen − *School of Optical and Electronic Information, Huazhong University of Science and Technology, Wuhan 430074, People's Republic of China; Optics Valley Laboratory, Wuhan 430074, People's Republic of China; Wuhan National Laboratory of Optoelectronics, Huazhong University of Science and Technology, Wuhan 430074, People's Republic of China*; orcid.org/0000-0001-7471-221X; Email: yuntian@hust.edu.cn

Authors

Jingwei Wang − *School of Optical and Electronic Information, Huazhong University of Science and Technology, Wuhan 430074, People's Republic of China*

Lida Liu − *School of Optical and Electronic Information, Huazhong University of Science and Technology, Wuhan 430074, People's Republic of China*

Yuhao Jing − *School of Optical and Electronic Information, Huazhong University of Science and Technology, Wuhan 430074, People's Republic of China*

Dominik Kowal − *Łukasiewicz Research Network - PORT Polish Center for Technology Development, Wrocław 54-066, Poland*; orcid.org/0000-0001-9424-0416

Complete contact information is available at: https://pubs.acs.org/10.1021/acsphotonics.4c02474

Funding

This work was supported by the National Natural Science Foundation of China (Grants No. 12274161), the Optics Valley Laboratory, Wuhan, Hubei 430074, China, and the Natural Science Foundation of Hubei Province of China under Grant 2024AFA016.

Notes

The authors declare the following competing financial interest(s): Y.C., J.W., L.L., and Y.J. have filed two patent applications related to the method discussed in this paper. These applications are currently under review. The details of these patent applications are as follows: CN118036372A and CN118036373A. These patents have not influenced the representation or interpretation of the reported research results.

■ REFERENCES

(1) Yu, N.; Capasso, F. Flat optics with designer metasurfaces. *Nat. Mater.* **2014**, *13*, 139−150.

(2) High, A. A.; Devlin, R. C.; Dibos, A.; Polking, M.; Wild, D. S.; Perczel, J.; de Leon, N. P.; Lukin, M. D.; Park, H. Visible-frequency hyperbolic metasurface. *Nature* **2015**, *522*, 192−196.

(3) Kodigala, A.; Lepetit, T.; Gu, Q.; Bahari, B.; Fainman, Y.; Kanté, B. Lasing action from photonic bound states in continuum. *Nature* **2017**, *541*, 196−199.

(4) Bag, A.; Neugebauer, M.; Mick, U.; Christiansen, S.; Schulz, S. A.; Banzer, P. Towards fully integrated photonic displacement sensors. *Nat. Commun.* **2020**, *11*, No. 2915.

(5) Shiratori, R.; Nakata, M.; Hayashi, K.; Baba, T. Particle swarm optimization of silicon photonic crystal waveguide transition. *Opt. Lett.* **2021**, *46*, 1904−1907.

(6) Torrijos-Morán, L.; Griol, A.; García-Rupérez, J. Slow light bimodal interferometry in one-dimensional photonic crystal waveguides. *Light:Sci. Appl.* **2021**, *10*, No. 16.

(7) Kang, M.; Liu, T.; Chan, C. T.; Xiao, M. Applications of bound states in the continuum in photonics. *Nat. Rev. Phys.* **2023**, *5*, 659−678.

(8) Rahman, B.; Davies, J. Penalty Function Improvement of Waveguide Solution by Finite Elements. *IEEE Trans. Microwave Theory Tech.* **1984**, *32*, 922−928.

(9) Nyakas, P. Full-Vectorial Three-Dimensional Finite Element Optical Simulation of Vertical-Cavity Surface-Emitting Lasers. *J. Lightwave Technol.* **2007**, *25*, 2427−2434.

(10) Wang, J.; Liu, L.; Jing, Y.; Xiong, Z.; Chen, Y. Efficient finite element modeling of photonic modal analysis augmented by combined symmetry. *Opt. Express* **2024**, *32*, No. 39245.

(11) Davies, J.; Fernandez, F.; Philippou, G. Finite Element Analysis of All Modes in Cavities with Circular Symmetry. *IEEE Trans. Microwave Theory Tech.* **1982**, *30*, 1975−1980.

(12) Bai, B.; Li, L. Group-theoretic approach to the enhancement of the Fourier modal method for crossed gratings: C_2 symmetry case. *J. Opt. Soc. Am. A* **2005**, *22*, 654−661.

(13) Garcia-Contreras, G.; Córcoles, J.; Ruiz-Cruz, J. A. Degeneracy-Discriminating Modal FEM Computation in Higher Order Rotationally Symmetric Waveguides. *IEEE Trans. Antennas Propag.* **2021**, *69*, 8003−8008.

(14) Mäntynen, H.; Lipsanen, H.; Anttu, N. Symmetry Reduction in FEM Optics Modeling of Single and Periodic Nanostructures. *Symmetry* **2021**, *13*, 752.

(15) Garcia-Contreras, G.; Córcoles, J.; Ruiz-Cruz, J. A. Rigorous Modal Characterization of First- and Second-Order Symmetric Waveguides Using Specular Periodic Boundary Conditions in 2D-FEM. *IEEE Trans. Antennas Propag.* **2022**, *70*, 10800−10810.

(16) Gladyshev, S.; Pashina, O.; Proskurin, A.; Nikolaeva, A.; Sadrieva, Z.; Petrov, M.; Bogdanov, A.; Frizyuk, K. Fast Simulation of Light Scattering and Harmonic Generation in Axially Symmetric Structures in COMSOL. *ACS Photonics* **2024**, *11*, 404−418.

(17) Ou, Y.; Pardo, D.; Chen, Y. Fourier finite element modeling of light emission in waveguides: 2.5-dimensional FEM approach. *Opt. Express* **2015**, *23*, 30259−30269.

(18) Wang, Z.; Wang, J.; Liu, L.; Chen, Y. Rotational Bloch Boundary Conditions and the Finite-Element Implementation in Photonic Devices. *Photonics* **2023**, *10*, No. 691.

(19) Wang, J.; Liu, L.; Wang, Z.; Jing, Y.; Chen, Y. Generalized Bloch boundary conditions based on a symmorphic space group and the finite-element implementation in photonic crystal. *J. Opt. Soc. Am. B* **2024**, *41*, 1031−1038.

(20) Aroyo, M. I.; Wondratschek, H. *International Tables for Crystallography*; John Wiley and Sons Limited, 2013.

(21) Xiong, Z.; Chen, W.; Wang, P.; Chen, Y. Classification of symmetry properties of waveguide modes in presence of gain/losses, anisotropy/bianisotropy, or continuous/discrete rotational symmetry. *Opt. Express* **2017**, *25*, 29822−29834.

(22) Heine, V. Group. Theory: Application to the Physics of Condensed Matter. *Phys. Today* **2008**, *61*, 57−58.

(23) Inui, T.; Tanabe, Y.; Onodera, Y. *Group Theory and its Applications in Physics*; Springer Science & Business Media, 2012; Vol. 78.

https://doi.org/10.1021/acsphotonics.4c02474
ACS Photonics 2025, 12, 2053−2061

(24) Jin, J.-M. *The Finite Element Method in Electromagnetics*; John Wiley & Sons, 2015.
(25) Wang, J.; Liu, L.; Jing, Y.; Xiong, Z.; Chen, Y. Symmetry adapted FEM for optical scattering problem. https://github.com/HUST-CPO/symmetry-FEM-for-optical-scattering-problem (accessed 20 Aug, 2024).
(26) Sinev, I. S.; Koshelev, K.; Liu, Z.; Rudenko, A.; Ladutenko, K.; Shcherbakov, A.; Sadrieva, Z.; Baranov, M.; Itina, T.; Liu, J.; Bogdanov, A. A.; Kivshar, Y. Observation of Ultrafast Self-Action Effects in Quasi-BIC Resonant Metasurfaces. *Nano Lett.* **2021**, *21*, 8848−8855.
(27) Hu, L.; Wang, B.; Guo, Y.; Du, S.; Chen, J.; Li, J.; Gu, C.; Wang, L. Quasi-BIC Enhanced Broadband Terahertz Generation in All-Dielectric Metasurface. *Adv. Opt. Mater.* **2022**, *10* (12), No. 2200193.
(28) Ha, S. T.; Fu, Y. H.; Emani, N. K.; Pan, Z.; Bakker, R. M.; Paniagua-Domínguez, R.; Kuznetsov, A. I. Directional lasing in resonant semiconductor nanoantenna arrays. *Nat. Nanotechnol.* **2018**, *13*, 1042−1047.
(29) Hwang, M.-S.; Lee, H.-C.; Kim, K.-H.; Jeong, K.-Y.; Kwon, S.-H.; Koshelev, K.; Kivshar, Y.; Park, H.-G. Ultralow-threshold laser using super-bound states in the continuum. *Nat. Commun.* **2021**, *12*, No. 4135.
(30) Zhang, X.; Liu, Y.; Han, J.; Kivshar, Y.; Song, Q. Chiral emission from resonant metasurfaces. *Science* **2022**, *377*, 1215−1218.
(31) Sang, Y.-G.; Lu, J.-Y.; Ouyang, Y.-H.; Luan, H.-Y.; Wu, J.-H.; Li, J.-Y.; Ma, R.-M. Topological polarization singular lasing with highly efficient radiation channel. *Nat. Commun.* **2022**, *13*, No. 6485.
(32) Heilmann, R.; Salerno, G.; Cuerda, J.; Hakala, T. K.; Törmä, P. Quasi-BIC Mode Lasing in a Quadrumer Plasmonic Lattice. *ACS Photonics* **2022**, *9*, 224−232.
(33) Xu, L.; Zangeneh Kamali, K.; Huang, L.; Rahmani, M.; Smirnov, A.; Camacho-Morales, R.; Ma, Y.; Zhang, G.; Woolley, M.; Neshev, D.; Miroshnichenko, A. E. Dynamic Nonlinear Image Tuning through Magnetic Dipole Quasi-BIC Ultrathin Resonators. *Adv. Sci.* **2019**, *6*, No. 1802119.
(34) Koshelev, K.; Tang, Y.; Li, K.; Choi, D.-Y.; Li, G.; Kivshar, Y. Nonlinear Metasurfaces Governed by Bound States in the Continuum. *ACS Photonics* **2019**, *6*, 1639−1644.
(35) Santiago-Cruz, T.; Gennaro, S. D.; Mitrofanov, O.; Addamane, S.; Reno, J.; Brener, I.; Chekhova, M. V. Resonant metasurfaces for generating complex quantum states. *Science* **2022**, *377*, 991−995.
(36) Zograf, G.; Koshelev, K.; Zalogina, A.; Korolev, V.; Hollinger, R.; Choi, D.-Y.; Zuerch, M.; Spielmann, C.; Luther-Davies, B.; Kartashov, D.; Makarov, S. V.; Kruk, S. S.; Kivshar, Y. High-Harmonic Generation from Resonant Dielectric Metasurfaces Empowered by Bound States in the Continuum. *ACS Photonics* **2022**, *9*, 567−574.
(37) Panmai, M.; Xiang, J.; Li, S.; He, X.; Ren, Y.; Zeng, M.; She, J.; Li, J.; Lan, S. Highly efficient nonlinear optical emission from a subwavelength crystalline silicon cuboid mediated by supercavity mode. *Nat. Commun.* **2022**, *13*, No. 2749.
(38) Chen, Y.; Zhao, C.; Zhang, Y.; Qiu, C.-w. Integrated Molar Chiral Sensing Based on High-Q Metasurface. *Nano Lett.* **2020**, *20*, 8696−8703.
(39) Jahani, Y.; Arvelo, E. R.; Yesilkoy, F.; Koshelev, K.; Cianciaruso, C.; De Palma, M.; Kivshar, Y.; Altug, H. Imaging-based spectrometer-less optofluidic biosensors based on dielectric metasurfaces for detecting extracellular vesicles. *Nat. Commun.* **2021**, *12*, No. 3246.
(40) Jacobsen, R. E.; Krasnok, A.; Arslanagić, S.; Lavrinenko, A. V.; Alú, A. Boundary-Induced Embedded Eigenstate in a Single Resonator for Advanced Sensing. *ACS Photonics* **2022**, *9*, 1936−1943.
(41) Gorkunov, M. V.; Antonov, A. A.; Kivshar, Y. S. Metasurfaces with Maximum Chirality Empowered by Bound States in the Continuum. *Phys. Rev. Lett.* **2020**, *125*, No. 093903.
(42) Chen, Y.; Deng, H.; Sha, X.; Chen, W.; Wang, R.; Chen, Y.-H.; Wu, D.; Chu, J.; Kivshar, Y. S.; Xiao, S.; Qiu, C.-W. Observation of intrinsic chiral bound states in the continuum. *Nature* **2023**, *613*, 474−478.
(43) Vaity, P.; Gupta, H.; Kala, A.; Dutta Gupta, S.; Kivshar, Y. S.; Tuz, V. R.; Achanta, V. G. Polarization-Independent Quasibound States in the Continuum. *Adv. Photonics Res.* **2022**, *3*, No. 2100144.
(44) Hopkins, B.; Poddubny, A. N.; Miroshnichenko, A. E.; Kivshar, Y. S. Circular dichroism induced by Fano resonances in planar chiral oligomers. *Laser Photonics Rev.* **2016**, *10*, 137−146.
(45) Chen, W.; Yang, Q.; Chen, Y.; Liu, W. Scattering activities bounded by reciprocity and parity conservation. *Phys. Rev. Res.* **2020**, *2*, No. 013277.
(46) Chen, W.; Yang, Q.; Chen, Y.; Liu, W. Extremize Optical Chiralities through Polarization Singularities. *Phys. Rev. Lett.* **2021**, *126*, No. 253901.
(47) Yang, Q.; Chen, W.; Chen, Y.; Liu, W. Symmetry Protected Invariant Scattering Properties for Incident Plane Waves of Arbitrary Polarizations. *Laser Photonics Rev.* **2021**, *15*, No. 2000496.
(48) Wen, C.; Zhang, J.; Zhang, C.; Qin, S.; Zhu, Z.; Liu, W. Chiroptical responses modulated by competitions between structural chiralities and magnetizations. *Phys. Rev. A* **2024**, *109*, No. 063502.
(49) Zhang, Y.; et al. Dynamics of polarization-tuned mirror symmetry breaking in a rotationally symmetric system. *Nat. Commun.* **2024**, *15*, No. 5586.
(50) Dorrah, A. H.; Rubin, N. A.; Zaidi, A.; Tamagnone, M.; Capasso, F. Metasurface optics for on-demand polarization transformations along the optical path. *Nat. Photonics* **2021**, *15*, 287−296.
(51) Liu, Y.; Weng, X.; Wang, M.; Li, W.; Ma, S.; Zhang, L.; Zhou, P.; Deng, L. Full Control of Fano Spectral Profile with GST-Based Metamaterial. *ACS Photonics* **2022**, *9*, 888−894.
(52) Ma, W.; Wen, Y.; Yu, X. Broadband metamaterial absorber at mid-infrared using multiplexed cross resonators. *Opt. Express* **2013**, *21*, 30724−30730.
(53) Li, W.; Xu, M.; Xu, H.-X.; Wang, X.; Huang, W. Metamaterial Absorbers: From Tunable Surface to Structural Transformation. *Adv. Mater.* **2022**, *34*, No. 2202509.
(54) Milias, C.; Andersen, R. B.; Lazaridis, P. I.; Zaharis, Z. D.; Muhammad, B.; Kristensen, J. T. B.; Mihovska, A.; Hermansen, D. D. S. Metamaterial-Inspired Antennas: A Review of the State of the Art and Future Design Challenges. *IEEE Access* **2021**, *9*, 89846−89865.
(55) Liu, Z.; Wang, D.; Gao, H.; Li, M.; Zhou, H.; Zhang, C. Metasurface-enabled augmented reality display: a review. *Adv. Photonics* **2023**, *5*, No. 034001.
(56) Kim, J.; Seong, J.; Yang, Y.; Moon, S.-W.; Badloe, T.; Rho, J. Tunable metasurfaces towards versatile metalenses and metaholograms: a review. *Adv. Photonics* **2022**, *4*, No. 024001.

https://doi.org/10.1021/acsphotonics.4c02474
ACS Photonics 2025, 12, 2053−2061